Femoral Bone Mesoscale Structural Architecture Prediction using Musculoskeletal and Finite Element Modelling

A.T.M. Phillips[a,b†], C. C. Villette[a,b], L. Modenese[a,c]

Affiliations:

[a]Structural Biomechanics, Department of Civil and Environmental Engineering, Imperial College London, London, UK

[b]The Royal British Legion Centre for Blast Injury Studies at Imperial College London, Imperial College London, London, UK

[c]Griffith Health Institute, Centre for Musculoskeletal Research, Griffith University, Gold Coast, Australia

Corresponding author:

[†]Dr Andrew Phillips, Structural Biomechanics, Department of Civil and Environment Engineering, Imperial College London, Skempton Building, South Kensington Campus, London SW7 2AZ, UK

Email: andrew.phillips@imperial.ac.uk

Telephone: +44 (0)207 594 6081

Original Article

Keywords: bone adaptation, structural optimisation, structure, architecture, femur, finite element, musculoskeletal

Short title: Bone Structural Architecture Prediction

The Version of Record of this manuscript has been accepted for publication and will be freely available in International Biomechanics 23 March 2015

http://www.tandfonline.com/10.1080/23335432.2015.1017609

Femoral Bone Mesoscale Structural Architecture Prediction using Musculoskeletal and Finite Element Modelling

A.T.M. Phillips, C.C. Villette, L. Modenese

27 February 2015

Abstract

Through much of the anatomical and clinical literature bone is studied with a focus on its structural architecture, while it is rare for bone to be modelled using a structural mechanics as opposed to a continuum mechanics approach in the engineering literature. A novel mesoscale structural model of the femur is presented in which truss and shell elements are used to represent trabecular and cortical bone respectively. Structural optimisation using a strain based bone adaptation algorithm is incorporated within a musculoskeletal and finite element modelling framework to predict the structure of the femur subjected to two loading scenarios; a single load case corresponding to the frame of maximum hip joint contact force during walking and a full loading regime consisting of multiple load cases from five activities of daily living. The use of the full loading regime compared to the single load case has a profound influence on the predicted trabecular and cortical structure throughout the femur, with dramatic volume increases in the femoral shaft and the distal femur, and regional increases at the femoral neck and greater trochanter in the proximal femur. The mesoscale structural model subjected to the full loading regime shows agreement with the observed structural architecture of the femur while the structural approach has potential application in bone fracture prediction, prevention and treatment. The mesoscale structural approach achieves the synergistic goals of computational efficiency similar to a macroscale continuum approach and a resolution nearing that of a microscale continuum approach.

1 Introduction

Bone structure and mechanics have been studied extensively, from as early as the 17^{th} century, when Galilei [1] proposed the dimensional scaling laws. The primary function of the skeletal system is the structural support of the body, while bone may adapt its geometry and structure to fulfil this function and resist the loads placed upon it [2]. Knowledge of skeletal structure is fundamental for assessment of the mechanical environment within the musculoskeletal system [3], which in turn may inform prediction, prevention and treatment of orthopaedic disorders as well as design of protective devices and prosthetics. Historically anatomists and engineers have observed the structure of trabecular bone in the proximal femur, hypothesising that it follows trajectories of compressive and tensile stress [4–7]. Comparisons have been made between the internal structure of a frontally sectioned proximal femur and the sketched stress trajectories of a curved (Fairbairn) crane [8]. It is generally accepted that bone adapts to its mechanical environment [4, 9, 10], leading to a structure optimised to withstand the forces acting on it (including muscle forces, joint contact forces and inertial loading) using a minimum volume of material. This study presents a predictive mesoscale structural model of the femur in which trabecular and cortical bone structure is optimised based on the strain environment present due to daily living activities.

1.1 Continuum modelling approaches

Finite element (FE) modelling using geometries and material properties extracted from medical imaging (typically computed tomography (CT) data) is a preferred tool for investigating the behaviour of bone at both macroscale [11] and microscale [12]. It is common at both the macroscopic and microscopic scales to model bone using solid continuum elements. A continuum model is considered to be either macroscale or microscale when the solid element size is larger or smaller respectively than the size of an individual structural component of bone such as a trabeculae [13, 14].

1.1.1 Macroscale continuum FE modelling

At the macroscale bone is considered as a continuum without voids, with material properties assigned across elements based on empirical relationships between CT attenuation values, density and Young's modulus [15, 16]. Macroscale continuum models can run in a matter of minutes on a standard workstation but present a limited resolution and typically overlook anisotropic material properties.

The macroscale continuum approach has been used in a number of studies in-

vestigating modelling [17, 18] and remodelling [19–21] of bone, using a variety of stress and strain stimuli to guide the bone apposition and resorption algorithm. Predictive studies have successfully extended the material constitutive relationship to include orthotropy and anisotropy in two-dimensional planar [22, 23] and three-dimensional spacial models of the femur [24].

1.1.2 Microscale continuum FE modelling

At the microscale bone is generally treated as a binary system with bone either being present or not. Homogeneous material properties are generally used although different values of Young's modulus may be adopted for cortical and trabecular bone [25]. The geometry of the model is typically derived from μCT or μMRI scans through thresholding on the attenuation values [26]. Although microscale models allow for fine resolution of bone structure, they are extremely computationally demanding, requiring multiple processors, and run times of several days. In addition, the significant radiation dose associated with current μCT acquisition technologies limits its application in-vivo [27].

The microscale continuum approach has been used in a small number of studies investigating modelling of the proximal femur [28–30], which found good agreement between predicted and observed trabecular bone trajectories. These studies generally used a limited number of simplified load cases to represent the varying mechanical environment present in the proximal femur due to a wide range of activities. As with microscale continuum models derived from μCT imaging, the predictive models provide a higher degree of resolution than macroscale continuum models at the cost of being extremely computationally demanding.

In addition to macroscale and microscale FE modelling approaches a small number of studies have investigated multiscale modelling approaches, where displacement distributions at the macroscale are used to drive modelling algorithms at the microscale [31, 32]. This approach has the advantage of increasing computational efficiency, although it does not result in a complete microscale model of the bone being investigated.

1.2 Structural modelling approaches

An alternative to both macroscale and microscale continuum FE modelling of bone is to adopt a structural FE modelling approach where a combination of idealized elements such as trusses, beams and shells are used to represent structural components of bone. At the microscale van Lenthe et al., [33] skeletonised a voxel-based μCT to produce corresponding structural and continuum models, the structural model being composed of individual or small groups of beams representing trabec-

ular bone. The structural model had a reduced CPU time by over a thousand fold compared to the continuum model, while results from both models were in excellent correlation ($R^2 = 0.97$).

Representing bone as a structure allows FE modelling to take place at the mesoscale, where individual structural elements may be larger than those found *in-vivo*, while being capable of capturing the overall structural behaviour of bone. The aim of this study was to develop a mesoscale structural model of the femur based on a physiological loading regime. With the exception of a small number of previous studies [34–37] FE models of the femur have utilised simplified boundary conditions and loading, resulting in non-physiological strain and stress distributions. In addition the majority of studies have utilised a single load case or a combined load case [17,18,22] to drive the bone adaptation algorithm. This approach fails to address the role of bone as a structure, required to resist the variety of load cases placed on it during daily living activities.

Hence two principal development stages are involved in the presented novel approach to predicting bone structural architecture in the femur. Firstly, an equilibrated set of loads (including muscle forces, joint contact forces (JCFs), and inertial loading) sampling five daily living activities was derived from an updated version of a validated musculoskeletal model [38]. It is believed that these simulations captured a fair representation of the physiological daily loading conditions experienced by the femur. Secondly, a strain-driven bone adaptation algorithm was used to optimise the bone structure subject to the derived loading regime. The resulting model was expected to be biofidelic, presenting a computational efficiency similar to macroscale continuum FE models and a spacial refinement approaching that of microscale continuum FE models.

2 Methods

The mesoscale structural model of the femur is obtained through iterative adaptation of a base FE model subject to a loading regime derived from musculoskeletal simulations of the following daily activities: walking, stair ascent and descent, sit-to-stand and stand-to-sit. The modelling framework is illustrated in Figure 1.

[Figure 1 about here.]

2.1 Musculoskeletal modelling

The load cases applied to the structural FE model were derived from musculoskeletal simulations of five daily living activities. Experimental data was collected on a volunteer (Male, age: 26 years, weight: 74 kg, height: 175 cm) for the purpose of

this study. The chosen activities: walking, stair ascent, stair descent, sit-to-stand and stand-to-sit are consistent with the frequent daily living activities identified by Morlock et al. [39] through the use of a portable monitoring system. Aspects of the musculoskeletal model that should be highlighted are the use of identical femoral geometry in both the musculoskeletal model and in the FE model in order to ensure that the load cases derived using the musculoskeletal model could be applied in the FE analysis as described in Section 2.2.1, and the use of an OpenSim plugin developed by the authors to extract muscle forces derived using the musculoskeletal model as vectors to be applied in the FE model [40] (available to download at https://simtk.org/home/force_direction).

The musculoskeletal model of the lower limb is based on the anatomical dataset published by Klein Horsman and colleagues [41] and implemented in *OpenSim* [42]. The ipsilateral model includes six segments (pelvis, femur, patella, tibia, hindfoot and midfoot plus phalanxes) connected by five joints (pelvis-ground connection, acetabulofemoral (hip) joint, tibiofemoral (knee) joint, patellofemoral joint and ankle joint). The pelvis is connected to ground with a free joint (6 degrees of freedom (DOF)), the hip is represented as a ball and socket joint (3 rotational DOF), the knee and ankle joints are modelled as hinges (1 DOF each) while the patella rotates around a patellofemoral axis as a function of the knee flexion angle. The patella ligament force was included in the model to allow force transmission between the patella and the tibia. 38 muscles of the lower extremity are represented through 163 actuators, whose path is enhanced by frictionless via points and wrapping surfaces. The local reference systems of the body segments were defined according to the recommendations of the International Society of Biomechanics [43]. The muscle attachment coordinates were the same as in Modenese et al. [38] for all segments except the femur, for which they were mapped directly onto a femoral mesh identical to the one used for the FE simulations. This operation was performed using NMSBuilder [44] and the visual guidance of anatomical atlases [45, 46] and the muscle standardized femur [47]. Additional wrapping surfaces were included to represent the hip joint capsule as in Brand et al. [48] and to prevent the quadriceps from penetrating the femur and to improve the gluteal muscle paths [49] as reported in van Arkel et al. [40]. The musculoskeletal model is shown during sit-to-stand in Figure 2.

[Figure 2 about here.]

Full body gait data was collected for a healthy volunteer with no history of joint pain or articular diseases, performing five daily living activities. The trajectories of 59 reflective markers positioned on bony landmarks and technical clusters were tracked using a *Vicon* system (Oxford Metrics, Oxford, UK) equipped with 10 infrared cameras. External forces (ground reaction forces (GRFs)) were measured using

three *Kistler* force plates (Type 9286BA, sampling rate 1000 Hz). An instrumented walkway was used for recording GRFs during walking (speed: 1.22 m/s, stride length: 1.29 m, cadence: 113.4 steps/minute). An instrumented staircase consisting of 3 steps (step height 15 cm and step depth 25 cm, resulting in an inclination of 36.8 degrees) was used for recording GRFs going upstairs and downstairs, with the three force plates placed on subsequent steps. A stool with a seat height of 50.7 cm from the floor was used for recording GRFs during sit-to-stand and stand-to-sit, with force plates placed at both feet and at the seat. All gait data was collected in the Biodynamics Lab in the Imperial College Research Labs at Charing Cross Hospital and processed using *Vicon Nexus* (Version 1.7.1) and the *Biomechanical ToolKit* [50].

The body segments of the musculoskeletal model were scaled to the anatomical dimensions of the volunteer by calculating ratios from lengths between sets of virtual and experimental markers; the inertial properties of the body segments were updated according to the regression equations of Dumas et al. [51]. Joint angles describing the motion for each of the investigated daily living activities were calculated from the experimental markers using an inverse kinematics approach [52]. Muscle forces were estimated by minimizing the sum of muscle activations squared for each frame of the kinematics under the constraints of joint moment equilibrium and physiological limits for the muscle forces [38, 53]. Finally JCFs were calculated at the hip, knee and patellofemoral joint. All musculoskeletal simulations were performed in *OpenSim* (Version 3.0.1) [42].

For each of the investigated activities, all loads acting on the femur were determined with respect to the segment reference system in order to be applied to the FE model. The inertial load and the gravitational force were calculated at the thigh centre of mass based on the segment kinetics, the joint contact forces were calculated at the joint centres using the *JointReaction* analysis tool available in *OpenSim* [54], while the femoral attachment point coordinates of each muscle actuator, together with the direction and magnitude of the muscle force, were extracted using the plugin developed by the authors [40].

2.2 Finite element base model

The base structural model of the femur was created using a similar methodology to Phillips [13]. A CT scan of a Sawbones fourth generation medium composite femur (#3403) was processed in *Mimics* to create a volumetric mesh composed of 113103 four-noded tetrahedral elements with an average edge length of 3.9 mm. The mesh was uniformly scaled to the femoral segment length required for the volunteer specific musculoskeletal model. The subsequent volumetric mesh was adapted using *Matlab* to create an initial structural mesh. The nodes and element faces of the

external surface of the volumetric mesh were used to define three-noded linear triangular shell elements, taken to be representative of cortical bone, with the external surface of the shell elements corresponding to the external geometry of the femur. These were arbitrarily assigned an initial thickness of 0.1 mm. Each of the internal nodes was considered in turn and used to define two-noded truss elements connecting between the node under consideration and the nearest sixteen neighbouring nodes, with the resulting network taken to be representative of trabecular bone. These were arbitrarily assigned a circular cross-section with an initial radius of 0.1 mm. With a minimum connectivity of sixteen at each node, it is believed that a sufficient range of element directionalities were available to allow region specific trabecular directionalities to develop during the bone adaptation process. It should be noted that while the minimum connectivity was sixteen the maximum was 42, mean 21.30 (SD 5.51). Figure 3 shows a 2.5mm thick slice of the proximal femur for the base model, composed of 10410 cortical shell elements and 218703 trabecular truss elements. Linear isotropic material properties were assigned for all elements, E=18000 MPa, ν=0.3 based on reported values for bone at the tissue level [55].

[Figure 3 about here.]

2.2.1 Loading

The muscle tensions estimated by the musculoskeletal model were applied as point loads at the nodes corresponding to the muscle insertion points in the FE model. JCFs and the inertial load, calculated at the joint centres and body segment centre of mass, were applied through specific constructs ('load applicators' and the 'inertia applicator') designed to spread the loads over the joint contact surfaces and the whole bone surface, respectively. The use of load applicators provides a significant reduction in CPU time in comparison with the inclusion of contact at the joint surfaces. The load applicators are shown in Figure 4.

[Figure 4 about here.]

The load applicators were composed of constructs made of four layers of six-noded linear continuum wedge elements superposed to the external surface of the appropriate regions of the base model. The load applicators, in combination with the surface elements of the base model, were taken to represent the bone-cartilage-cartilage-bone interfaces at the joints. They were generated through the projection of the nodes of the regions of interest along the direction defined by the considered nodes and the centre of the joint, directed outwards. The thickness of each of the layers was 1 mm. The bottom two layers, taken to represent cartilage, were assigned E=10 MPa, $\nu = 0.49$. The top two layers were assigned stiffer material properties;

bone for the acetabulofemoral (hip) and tibiofemoral (knee) joints and a one order of magnitude softer material (E=1800 MPa, ν=0.3) for the patellofemoral joint (the patella as a sesamoid bone embedded in ligament is considered to be less stiff than the acetabular and tibial joint surfaces).

The hip joint presents three rotational DOF, hence it will transfer forces but not moments. The acetabulofemoral load applicator was hence completed by connecting each of the external nodes of the applicator to the centre of the joint (as defined in the musculoskeletal model) using truss elements. The JCFs derived from the musculoskeletal simulations were applied at the centre of the joint. The knee and patellofemoral joints each present a single rotational DOF, hence moments may be transferred at both joints about the directions perpendicular to their rotation axes. In order to facilitate the transfer of moments at the knee and patellofemoral joints without introducing local moment transfer between the load applicators and the underlying bone, moments were applied via force couples on two points located on the joint axes either side of the respective joint centres (as defined in the musculoskeletal model). The definition of the hip and knee joint load applicators corresponds to the respective joint contact surfaces, over the range of motion for all activities. To allow for patella movement across the surface of the femur during knee flexion, the patellofemoral load applicator was defined as a band passing between the two condyles prolongated over the distal portion of the frontal shaft. The tibiofemoral and patellofemoral load applicators were completed in a similar manner to the acetabulofemoral load applicator, by connecting each of the external nodes of the applicator to each of the points on the respective joint axes. Truss elements for all of the load applicators were given a circular cross section with a radius of $2.5mm$ (similar to the edge length of the surface elements). The hip and knee joint trusses were assigned the material properties of bone (E=18000 MPa, ν=0.3). For consistency with the top two layers of the load applicator, the patellofemoral trusses were assigned a one order of magnitude softer material (E=1800 MPa, ν=0.3).

An 'inertia applicator' was designed based on the same concept as the load applicators. It is composed of soft truss elements (radius: 2.5 mm, E=5 MPa, ν=0.3) linking every node of the femoral surface with the centre of mass of the leg, where the inertial load is applied. Young's modulus was set to a low value to ensure that stiffening of the model was negligible. The use of a higher value could result in reduced deformation along the length of the femur. Spreading the inertial load over the whole volume rather than the surface was considered, but ruled out at this stage due to the severe increase in CPU time (up to a five times higher) involved.

Loading conditions from a subset of frames, derived from the musculoskeletal model, representative of each activity were selected to increase the computational efficiency of the FE model. Frame selection was done using an 'integration limit error' approach based on the hip JCF. The evolution of the hip JCF was inte-

grated using the trapezoidal method on the full set of frames. Frames were then successively removed from the sample and the corresponding integration between remaining frames compared to that obtained from the full frame set. The process was repeated until no further frames could be removed without generating a difference in integration between two adjacent sampled frames of more than 1% of the integration of the full frame set. Figure 5 shows the selected frames as well as the hip JCF derived from the musculoskeletal model, alongside the average hip JCF as reported by Bergmann et al. [56] for the same activities, for comparison. The magnitudes of the predicted hip JCFs for all activities were found to be within the ranges recorded by Bergmann et al. [56], with the exception of the second peak during walking, which was higher for the musculoskeletal model. A direct comparison is difficult as the hip JCFs derived from the musculoskeletal model are for a young healthy subject (26 years), while those recorded by Bergmann et al. [56] are for four older patients (51–76 years) who had undergone hip replacement surgery.

[Figure 5 about here.]

The load cases (including muscles forces, JCFs and inertia forces) corresponding to the selected time frames of the different activities were applied in consecutive analysis steps of the FE simulation.

2.2.2 Boundary conditions

Specific 'fixator' constructs were designed at the acetabulofemoral and the tibiofemoral joints to allow boundary conditions compatible with the DOF present in the musculoskeletal model to be applied, based on the same concept as load applicators. The acetabulofemoral fixator consists of truss elements linking the nodes of the external surface of the acetabulofemoral load applicator back to a point superposed with the centre of the hip joint. The tibiofemoral fixator consists of truss elements linking the nodes of the external surface of the tibiofemoral load applicator back to two points superposed with the force couple points on the knee joint axis described previously. From consideration of the musculoskeletal model, it is clear that no moment can develop at the centre of the hip joint, nor about the knee joint axis. Hence the centre of the acetabulofemoral joint was restrained against displacement along any of the three femoral axes [43]. At the tibiofemoral joint the medial of the two points on the joint axis was restrained against displacement in the plane perpendicular to the joint axis, while the lateral of the two points was restrained against displacement in the direction corresponding to the cross-product of the vectors defining the joint axis and the femoral X-axis (anterior-posterior) [43]. Thus the FE model was restrained against translation in the minimum number of DOF (six) required to define a stable structure. It should be noted that although

the points of load application and points of restraint application were coincident in space for the undeformed model, they were defined as separate points, which displaced with respect to each other when the model was subjected to load. Truss elements for both of the fixators were given a circular cross section with a radius of $2.5mm$ and material properties, E=1000 MPa, ν=0.3. The modulus of the fixator trusses was set one order of magnitude lower than than the modulus of the load applicator trusses in order to prevent artificial stiffening of the model close to the joint surfaces.

2.3 Bone adaptation algorithm

Adopting the Mechanostat hypothesis [10] successive iterations of the base model were subjected to the loading regime derived from the musculoskeletal model, with the cross-sectional area of each truss element and the thickness of each shell element adjusted with each iteration according to the resulting strain environment. The iterative process was controlled using a combination of *Matlab* and *Python* scripts, while successive FE models were run using the *Abaqus/Standard* solver, until convergence was achieved.

For the i^{th} iteration the maximum absolute strain for the j^{th} truss and the j^{th} shell element over $\lambda = 1, \ldots, n$ load cases was defined using Equations 1 and 2 respectively:

$$|\epsilon_{i,j}|_{\max} = \max\left(|\epsilon_{11,j,\lambda}|\right) \tag{1}$$

where $\epsilon_{11,j,\lambda}$ is the axial strain in the j^{th} truss element for the load case λ.

$$|\epsilon_{i,j}|_{\max} = \max\left(|\epsilon^{t}_{\max,j,\lambda}|, |\epsilon^{t}_{\min,j,\lambda}|, |\epsilon^{b}_{\max,j,\lambda}|, |\epsilon^{b}_{\min,j,\lambda}|\right) \tag{2}$$

where $\epsilon^{t}_{\max,j,\lambda}$, $\epsilon^{t}_{\min,j,\lambda}$ and $\epsilon^{b}_{\max,j,\lambda}$, $\epsilon^{b}_{\min,j,\lambda}$ are the maximum and minimum principal strains in the top and bottom surfaces respectively of the j^{th} shell element for the load case λ.

The adopted strain ranges associated with the dead zone, bone resorption, the lazy zone and bone apposition [10, 13] are given in Equation 3.

$$\phi_{i,j} = \begin{cases} 0, & \text{for } 0 \leq |\epsilon_{i,j}|_{\max} \leq 250\mu\epsilon & \text{(Dead zone)} \\ 1, & \text{for } 250 < |\epsilon_{i,j}|_{\max} < 1000\mu\epsilon & \text{(Bone resorption)} \\ 0, & \text{for } 1000 \leq |\epsilon_{i,j}|_{\max} \leq 1500\mu\epsilon & \text{(Lazy zone)} \\ 1, & \text{for } |\epsilon_{i,j}|_{\max} > 1500\mu\epsilon & \text{(Bone apposition)} \end{cases} \tag{3}$$

For the $(i+1)^{\text{th}}$ iteration the cross-sectional area, A of the j^{th} truss element and the thickness, T of the j^{th} shell element were adjusted according to Equations 4 and 5 respectively, adopting a target strain, ϵ_t of $1250\mu\epsilon$, at the centre of the lazy

zone. The target strain and range of the lazy zone were considered reasonable based on in-vivo surface strain measurements on the human femur, taken below the greater trochanter by Aamodt et al. [57] for two subjects during single leg stance, walking and stair climbing, finding peak values in the range of 1000 to 1500 $\mu\epsilon$ across all activities.

$$\begin{aligned} &\text{if } \phi_{i,j} = 1, \quad A_{i+1,j} = A_{i,j}\frac{|\epsilon_{i,j}|_{\max}}{\epsilon_t} \\ &\text{else} \qquad\quad A_{i+1,j} = A_{i,j} \end{aligned} \tag{4}$$

$$\begin{aligned} &\text{if } \phi_{i,j} = 1, \quad T_{i+1,j} = \frac{T_{i,j}}{2}\left(1 + \frac{|\epsilon_{i,j}|_{\max}}{\epsilon_t}\right) \\ &\text{else} \qquad\quad T_{i+1,j} = T_{i,j} \end{aligned} \tag{5}$$

Equation 5 compared to Equation 4 preferences adaptation of trabecular bone compared to cortical bone over each individual iteration. This was done to avoid oscillation of the predicted thickness values of the shell elements representing cortical bone during the initial iterations of the FE simulation.

With the aim of reducing the complexity of the model, hence increasing its computational efficiency, the trabecular cross-sectional area and shell cortical thickness domains were linearly discretised into 255 and 256 categories respectively. The trabecular cross-sectional area was discretised between lower and upper limits corresponding to circular cross-sections of radii 0.1 mm and 2 mm (cross sectional areas of $\pi(0.1)^2$ mm^2 and $\pi(2)^2$ mm^2). This range was considered to correlate on the mesoscale with bone volume fraction measurements (the ratio of bone volume to total volume (BV/TV)) recorded for trabecular bone samples using μCT [14]. The cortical thickness was discretised between lower and upper limits of 0.1mm and 8mm [58, 59]. Based on $A_{i+1,j}$ or $T_{i+1,j}$ each element was assigned the cross-sectional area or thickness value corresponding to the closest discrete value of the respective truss and shell domains.

For the trabecular truss elements a 256$^{\text{th}}$ discrete circular cross-section was added with a radius of 1μm, allowing for effective removal of elements from the model, making their stiffness contribution to the model negligible while maintaining numerical stability, subject to Equation 6.

$$\text{if } A_{i,j} = \pi(0.1)^2 \;\&\; |\epsilon_{i,j}|_{\max} \leq 250\mu\epsilon, \;\; A_{i+1,j} = \pi(0.001)^2 \tag{6}$$

These elements were allowed to regenerate subject to Equation 7.

$$\text{if } A_{i,j} = \pi(0.001)^2 \;\&\; |\epsilon_{i,j}|_{\max} \geq 2500000\mu\epsilon, \;\; A_{i+1,j} = \pi(0.1)^2 \tag{7}$$

where the value of 2500000$\mu\epsilon$ was decided based on the ratio of cross-sectional areas for radii of 0.1mm and 1μm

3 Results

Figures 6 and 7 show a selection of 5 mm thick slices through the converged mesoscale femoral structural architecture for the model subjected to a single load case taken at the maximum hip JCF during walking and the model subjected to the full loading regime described in section 2.2.1 respectively. It can be seen that the structure is more substantial in the full loading regime model, compared to the single load case model, in particular in the distal region of the femur.

[Figure 6 about here.]

[Figure 7 about here.]

The resulting bone architectures for the single load case and the full loading regime models were compared to literature and μCT imaging available to the authors. Figure 6 shows that in the proximal femur a substantial proportion of the clinically observed architecture can be predicted based on a single load case. Figure 8 highlights the five normal groups of trabeculae identified by Singh et al. [60] for the frontal proximal slice shown in Fig. 6a). Ward's triangle [60, 61] can also be seen. The cortex at the hip joint and at the greater trochanter is thin, thickening in the shaft and the inferior femoral neck as expected from clinical observations. The arched arrangement of trabeculae in the proximal metaphysis is clear, consistent with Garden [62]. Truss elements with a radius of 0.1 mm are clustered at the hip joint surface allowing force transfer perpendicular to the cortex. In the femoral shaft it is observed that the single load case (Fig. 6c-g) provides a reasonable prediction of cortical thickness in the medial and lateral aspects, but a poor prediction in the anterior and posterior aspects compared to clinical observations [58, 59]. A number of large trabecular elements running parallel to the femoral shaft are observed within the thickness of the cortex on the medial and lateral aspects, while a number of smaller trabecular elements are observed running perpendicular to the femoral shaft in the anterior and posterior aspects. These results are consistent with the femur bending about the anterior-posterior axis during walking. In the distal femur for the model subjected to the single load case (Fig. 6h-i) the trabecular structure is sparse in comparison to clinical observations [63]. However the structural architecture that is observed in the transverse plane in particular (Fig. 6i) is consistent with the principal trabeculae group reported by Takechi [63] with trabeculae originating from the posterior condyle and patella articular surfaces, arranged close to parallel to the medial and lateral perimeter surfaces of the condyles.

[Figure 8 about here.]

Comparing the structural architecture of the proximal femur obtained with a single load case (Fig. 6a-b) to that obtained with the full loading regime (Fig 7a-b) it is observed that the full loading regime results in increased trabecular architecture in the femoral neck and greater trochanter in particular. Figure 9 shows for the same selection of slices which of the daily loading activities is most influential over the structural architecture in different regions of the model subjected to the complete loading regime.

[Figure 9 about here.]

The activity mapping (Fig. 9a-b) indicates that walking and stair ascent are primary responsible for the thickness of the cortex in the femoral neck, while stair ascent and stand-to-sit are responsible for the increase in the trabecular structure in the femoral neck compared to the frame of maximum hip JCF during walking alone. The additional structure in the greater trochanter region is influenced by stair descent and stand-to-sit activities. Of particular note is the increased cortical thickness in the anterior aspect of the greater trochanter region due to stand-to-sit and to a lesser extent sit-to-stand. Comparing the predicted structural architecture in the femoral shaft for the single load case (Fig. 6c-g) and the full loading regime (Fig. 7c-g) it is observed that the inclusion of additional load cases causes a thickening of the cortex as well as the development of an increased number of large trabecular elements running perpendicular to the femoral shaft in the anterior and posterior aspects. The activity mapping (Fig. 9c-g) indicates that walking influences the thickness of the medial cortex throughout the majority of the femoral shaft, stair ascent influences the cortex thickness in the anterior, posterior and lateral aspects through various regions of the femoral shaft, while stair descent and sit-to-stand have increasing influence in the distal region of the femoral shaft. The results are consistent with the addition of activities which place the knee in flexion causing bending about the medial-lateral axis. In the distal femur the full loading regime (Fig. 7h-i) is seen to produce a considerable increase in the trabecular architecture in comparison to the single load case (Fig. 6h-i). The activity mapping (Fig. 9h-i) indicates that sit-to-stand and stand-to-sit have a significant influence over the trabecular architecture of the distal femur, with sit-to-stand causing the development of trabeculae in the lateral condyle in particular. It is observed that many of the trabeculae associated with stand-to-sit run perpendicular to the main trabecular structure providing additional stiffness to the structure as a whole. For the full loading regime in particular, a large number of trabecular elements with $r = 0.1mm$ are observed in the femoral shaft (Fig. 6c-g). It is thought that this is due to the dead zone limit being set at $250\mu\epsilon$. Although not shown here there was a significant reduction in the occurrence of these elements when the limit was raised to reduce the range between the dead zone and the lazy zone.

4 Discussion

There are a preponderance of studies, several of which are referenced in this work, which focus on adaptation of the proximal femur under a single or combined load case. As discussed by Skedros and Baucom [8] it may be suggested that there has been 'an unfortunate historical emphasis on the human proximal femur' with the role of multiple load cases in influencing the structural architecture of the femur obfuscated. The results of this work indicate that the inclusion of a range of daily living activities has a profound influence on the predicted architectural structure not only of the distal femur but also of the femoral shaft and regions of the proximal femur.

It is observed in Figs. 7 and 9 that in certain regions of the converged structural model trabecular truss elements are enclosed within the volume of cortical shell elements. In order to compare the converged full loading regime model with μCT images the visual thickness of the cortex in these regions was altered in order to incorporate the volume of material contained in the enclosed trabecular elements. Figure 10 shows proximal and distal slices of the altered cortical thickness model alongside equivalent μCT slices for an adult male.

[Figure 10 about here.]

Examining the coronal slices of the proximal (Fig. 10a-b) and distal femur (Fig. 10c-d) it can be seen that the predicted structure compares favourably to the observed structure in the proximal region, while the comparison is not as favourable for the distal femur. There is a sparse trabecular structure beneath the trochlear grove in the μCT slice, while the same region in the predicted model has a quite a dense trabecular architecture. This may be due to the specific implementation of the patellofemoral load applicator. In future work the design of the patellofemoral load applicator will be altered to better represent separate areas of patella contact on the two sides of the articular surface. The absence of knee ligaments in the musculoskeletal and FE models is also highlighted, potentially resulting in the scant trabecular structure at the medial and lateral perimeters of the condyles seen in the predicted model compared to the μCT slice. The superior part of the femoral head has a denser structure in the μCT slice than the predicted model. This may be due to large area for force transfer provided by the hip load applicator which surrounds the femoral head in the FE model, while the contact area between the femoral head and the acetabulum during each activity will be smaller in practice. In the slices running parallel to the femoral neck (Fig. 10e-f) there is remarkable agreement in the cortical thickness distribution between the predicted model and the μCT observations, while the trabecular architectural arrangement is similar between the two

slices. In the distal transverse plane slices (Fig. 10g-h) the trabecular arrangement shows similarities between the predicted model and the μCT slice, although the trajectories are more pronounced in running parallel to the perimeter of the condyles in the μCT slice. This may also be related to the design of the patellofemoral load applicator with the trabeculae focusing towards the trochlear groove in the predicted model. Quantitative comparison between the predicted model and the μCT observations is impractical due to the difference in geometries between the two femurs and the difficult in selecting equivalent corresponding slices. However, with the exceptions described, it can be seen that there is reasonable agreement between the predicted and observed trabecular and cortical structural architecture.

The converged mesoscale structural model was found to have a low computational cost (229113 elements, 77229 design variables (nodal DOF), with a run time of 52 seconds on a workstation PC with two Intel Xeon E5-2603 1.80GHz processors and 16GB of RAM). The adaptation run times for the model subjected to a single load case and the full loading regime, were around 1 hour and 10 hours, respectively. Although run times are not reported, Tsubota et al. [29] developed microscale models of the proximal femur with around 12 million elements at a 175μm resolution, and around 93 million elements at a 87.5μm resolution, reporting converged structures visually similar to those found using the mesoscale structural model. Boyle and Kim [30] developed a similar microscale model of the proximal femur, utilising around 23.3 million elements at a 175μm resolution, equivalent to around 15.7 million design variables. Subjecting the model to a single combined load case they reported an adaptation run time of around 343 hours on a computing cluster. Although the presented structural model has not been implemented at the microscale it seems reasonable to conclude that it is efficient, with a low computational cost in comparison to microscale continuum models, while providing an improved structural representation in comparison to a macroscale continuum model with a similar number of design variables. In future work potential efficiency gains may be realised by generating an initial structural model, with fewer elements, based on stress and strain tensors found using a macroscale continuum model, aligning structural elements with principal stress directions, and basing initial sizing on principal strain values [24].

A number of limitations must be acknowledged in the study. While some of these are associated with the use of the structural modelling approach many are generic to the utilisation of musculoskeletal and finite element modelling methodologies [64, 65] in the combined modelling approach. While the approach is considered to provide a more physiological mechanical environment, compared to models in which simplified boundary conditions and loading are utilised, deficiencies are exposed in both modelling methodologies through the process of developing corresponding models in both. The development of load applicators, fixators and application

of corresponding boundary conditions in the finite element model highlight the assumptions made in the development of the musculoskeletal model, treating the tibiofemoral and patellofemoral joints as hinges, with the position of the patella depending on the knee flexion angle, omitting the possibility of displacements in other degrees of freedom.

It has been demonstrated in previous studies of the femur that inclusion of physiological loading [19,35] and boundary conditions [37] is crucial for bone adaptation simulations as they have a significant influence on the resulting mechanical fields. Deriving the load cases for the FE simulation from a musculoskeletal model with an identical femoral geometry is therefore seen as essential and appropriate in the context that the estimated JCFs (Fig. 5) are of comparable magnitude to those measured using instrumented hip prostheses [56] while the activation profiles found using the original musculoskeletal model [38] are similar to measured electromyographic profiles. However, a limitation of the combined modelling approach is the use of an equilibrated load set, derived from a rigid multibody system, applied to a deformable FE model, with displacement compromising the equilibrium condition.

While wrapping surfaces and via points in the musculoskeletal model allow for a more physiological representation of muscles paths, compared to a straight line approach, they are not replicated as constructs in the finite element model, resulting in a further compromise of the equilibrium condition. When a muscle force is applied in the FE simulations a choice must be made between using the 'anatomical' line of action (originating from the muscle attachment on the bone surface) or the 'effective' line of action (originating off the bone surface, which determines its mechanical effect on the joints and its contribution to the equilibrium equations [66]). This choice of muscle lines of action is illustrated for the gastrocnemius medialis muscle in Figure 11. In this work the anatomical lines of action were used. In future work the authors plan to incorporate wrapping surface constructs within the finite element model in order to facilitate the transfer of compressive and traction muscle loading to the bone [67, 68]. It is hypothesised that this will provide an improved strain environment with which to drive the bone adaptation algorithm and allow the use of the use of the effective line of action avoiding violation of the equilibrium condition. Although other studies have for a range of anatomical constructs used similar methodologies to that described here [35, 64, 69, 70], this limitation was either inapplicable due to the absence of wrapping surfaces or not explicitly discussed.

[Figure 11 about here.]

The principal limitation of the structural modelling approach as applied in this study is the use of truss elements to represent trabecular bone, in preference to beam elements, or a combination of beam and shell elements. The decision to use truss

elements was considered reasonable as under loading an optimised structure can be expected to maximise axial forces while minimising bending moments and shear forces, as these are less efficiently resisted through the cross-section of a structural element, while truss elements are computationally efficient in comparison to beam elements. In order to assess the effect of using truss rather than beam elements the converged model was adapted by replacing the truss elements in turn with two-noded hermite-cubic Euler-Bernoulli beam elements and three-noded quadratic Timoshenko elements, with the third node placed at the midpoint of the element. The original and adapted versions of the converged model were then subjected to a simplified load case, with a distributed vertical load applied at the femoral head, and fixed boundary conditions applied at the knee joint. The displacement in both the beam models was found to be 1.4% greater than the displacement in the truss model, while all three models deformed in a similar manner. The Timoshenko and Euler-Bernoulli beam models had run times of 214 and 189 seconds respectively, on the workstation PC. A limitation of the structural model, albeit one that is inherent to the majority of phenomenological bone adaptation studies, is the adoption of particular values for the target strain, the lazy zone and the dead zone. It is possible that these values should be varied for different regions of the skeletal system, while they may also be influenced by a multitude of factors including age, sex, ethnicity, and disease conditions such as osteoarthritis and osteoporosis. An additional limitation of the structural model is the adoption of particular ranges for the trabecular cross-sectional area and the cortical thickness. While the range of cortical thickness may be justified by comparison to clinical observations [58, 59] the range of trabecular cross-sectional area was considered reasonable given the mesoscale nature of the model. Future work will assess the application of the approach at the microscale. The development of a microscale structural model with physiological length and thickness ranges [14, 71] for individual trabeculae will allow for direct comparison with μCT data.

A robust structural approach to bone adaptation has been presented as part of a combined musculoskeletal and finite element modelling framework. Future work will extend the approach to the other skeletal structures of the lower limb including the pelvis [72]. The work has highlighted the importance of including multiple load cases in bone adaptation studies, with a range of daily loading activities influencing the structural architecture of different regions of the femur. It is believed that the work has relevance to the study and potential treatment of diseases of the musculoskeletal system including osteoporosis and osteoarthritis. As an example the risk of femoral neck fracture in osteoporosis may be reduced by introducing additional activities, other than walking, promoting bone structure formation in the femoral neck, into a protective exercise regime [73]. Preliminary work by the authors has also indicated that the structural approach has application in the computationally

efficient modelling of fracture initiation and progression due to traumatic loading such as that experienced during falls or jumps from height, vehicular collision, and blast injury.

The development of a mesoscale structural model, rather than a continuum model, allows for additive manufacturing of the resulting structure. With suitable manipulation of the bone adaptation algorithm, 3D printing in materials including a wide range of polymers and metals, permits the manufacture of frangible bone simulants for use in experimental testing, as well as the potential design and manufacture of bioresorbable scaffolds and orthopaedic implants, sympathetic to the remaining skeletal structural architecture.

5 Acknowledgements

The authors acknowledge and appreciate funding from the Royal British Legion Centre for Blast Injury Studies at Imperial College London, and the Engineering and Physical Sciences Research Council through a Doctoral Training Award and a Project Award (EP/F062761/1). The authors thank the Human Performance and Musculoskeletal Biomechanics groups at Imperial College London for assistance with the gait analysis, and Imperial Blast for providing the μCT data. The authors thank the volunteer. The authors acknowledge and thank Alfred Thibon for the work carried out during his MSc Dissertation in the Department of Civil and Environmental Engineering at Imperial College London, which assisted in developing the work presented here.

References

[1] G. Galilei. *Discorsi e dimostrazioni matematiche intorno a due nuove scienze*. The Macmillan Company, 1638. Dialogues Concerning Two New Sciences, Translation by Henry Crew and Alfonso de Salvio, available at oll.libertyfund.org/titles/galilei-dialogues-concerning-two-new-sciences.

[2] T. G. Toridis. Stress analysis of the femur. *Journal of biomechanics*, 2(2):163–174, 1969.

[3] M. Viceconti. *Multiscale Modeling of the Skeletal System*. Cambridge University Press, 2011. ISBN-13: 978-0521769501.

[4] J. Wolff. Über die bedeutung der architektur des spongisen substanz. *Zentralblatt für die medizinischen Wissenschaft*, 54:849851, 1869. Translated and publised as a classic article available at doi:10.1007/s11999-011-2041-5.

[5] K. Culmann. *Die graphische statik*. Meyer & Zeller, 1866. Available from books.google.co.uk/books?id=Ab8KAAAAIAAJ.

[6] H. von Meyer. Die architektur der spongiosa. *Archiv für Anatomie, Physiologie und Wissenschaftliche Medicin*, 34:615–628, 1867. Translated and published as a classic article available at doi:10.1007/s11999-011-2042-4.

[7] J. Koch. The laws of bone architecture. *American Journal of Anatomy*, 21(2):177–298, 1917. doi:10.1002/aja.1000210202.

[8] J. G. Skedros and S. L. Baucom. Mathematical analysis of trabecular 'trajectories' in apparent trajectorial structures: the unfortunate historical emphasis on the human proximal femur. *Journal of theoretical biology*, 244(1):15–45, 2007. doi:10.1016/j.jtbi.2006.06.029.

[9] J. Wolff. *The law of bone remodelling*. Springer-Verlag Berlin, 1986. Translated from by Paul Maquet Ronald Furlong, ISBN-13: 978-3642710339.

[10] H. M. Frost. Bone's mechanostat: a 2003 update. *The Anatomical Record Part A: Discoveries in Molecular, Cellular, and Evolutionary Biology*, 275(2):1081–1101, 2003. doi:10.1002/ar.a.10119.

[11] F. Taddei, S. Martelli, B. Reggiani, L. Cristofolini, and M. Viceconti. Finite-element modeling of bones from CT data: sensitivity to geometry and material uncertainties. *IEEE Transactions on Bio-medical Engineering*, 53(11):2194–2200, 2006. doi:10.1109/TBME.2006.879473.

[12] R. Hambli. Micro-CT finite element model and experimental validation of trabecular bone damage and fracture. *Bone*, 56:363–374, 2013. doi:10.1016/j.bone.2013.06.028.

[13] A. T. M. Phillips. Structural optimisation: biomechanics of the femur. *Engineering and Computational Mechanics*, 165:147–154, 2012. doi:10.1680/eacm.10.00032.

[14] E. Nägele, V. Kuhn, H. Vogt, T. Link, R. Müller, E.-M. Lochmüller, and F. Eckstein. Technical considerations for microstructural analysis of human trabecular bone from specimens excised from various skeletal sites. *Calcified Tissue International*, 75(1):15–22, 2004. doi:10.1007/s00223-004-0151-8.

[15] D. R. Carter and W. C. Hayes. The compressive behaviour of bone as a two-phase porous structure. *Journal of Bone and Joint Surgery. American Volume*, 59(7):954–962, 1977. PMID: 561786.

[16] B. Helgason, E. Perilli, E. Schileo, F. Taddei, S. Brynjólfsson, and M. Viceconti. Mathematical relationships between bone density and mechanical properties: a literature review. *Clinical Biomechanics*, 23(2):135–146, 2008. doi:10.1016/j.clinbiomech.2007.08.024.

[17] G. S. Beaupré, T. E. Orr, and D. R. Carter. An approach for time-dependent bone modeling and remodeling — theoretical development. *Journal of Orthopaedic Research*, 8(5):651–661, 1990. doi:10.1002/jor.1100080506.

[18] G. S. Beaupré, T. E. Orr, and D. R. Carter. An approach for time-dependent bone modeling and remodeling — application: A preliminary remodeling simulation. *Journal of Orthopaedic Research*, 8(5):662–670, 1990. doi:10.1002/jor.1100080507.

[19] C. Bitsakos, J. Kerner, I. Fisher, and A. A. Amis. The effect of muscle loading on the simulation of bone remodelling in the proximal femur. *Journal of Biomechanics*, 38(1):133–139, 2005. doi:10.1016/j.jbiomech.2004.03.005.

[20] R. Huiskes, H. Weinans, H. Grootenboer, M. Dalstra, B. Fudala, and T. Slooff. Adaptive bone-remodeling theory applied to prosthetic-design analysis. *Journal of Biomechanics*, 20:1135–1150, 1987. doi:10.1016/0021-9290(87)90030-3.

[21] J. García-Aznar, T. Rueberg, and M. Doblare. A bone remodelling model coupling micro-damage growth and repair by 3D BMU-activity. *Biomechanics and modeling in mechanobiology*, 4(2-3):147–167, 2005. doi:10.1007/s10237-005-0067-x.

[22] Z. Miller, M. B. Fuchs, and A. Mircea. Trabecular bone adaptation with an orthotropic material model. *Journal of Biomechanics*, 35:247–256, 2002. doi:10.1016/S0021-9290(01)00192-0.

[23] M. Doblaré and J. M. Garćia. Application of an anisotropic bone-remodelling model based on a damage-repair theory to the analysis of the proximal femur before and after total hip replacement. *Journal of Biomechanics*, 34:1157–1170, 2001. doi:10.1016/S0021-9290(01)00069-0.

[24] D. M. Geraldes and A. T. M. Phillips. A comparative study of orthotropic and isotropic bone adaptation in the femur. *International Journal for Numerical Methods in Biomedical engineering*, 30:873–889, 2014. doi:10.1002/cnm.2633. In press, accepted manuscript.

[25] E. Verhulp, B. van Rietbergen, and R. Huiskes. Comparison of micro-level and continuum-level voxel models of the proximal femur. *Journal of biomechanics*, 39(16):2951–2957, 2006. doi:10.1016/j.jbiomech.2005.10.027.

[26] D. Ulrich, B. Van Rietbergen, H. Weinans, and P. Regsegger. Finite element analysis of trabecular bone structure: a comparison of image-based meshing techniques. *Journal of biomechanics*, 31(12):1187–1192, 1998. doi:10.1016/S0021-9290(98)00118-3.

[27] P. Pankaj. Patient-specific modelling of bone and bone-implant systems: the challenges. *International Journal for Numerical Methods in Biomedical engineering*, 29:233–249, 2013. doi:10.1002/cnm.2536.

[28] I. G. Jang and I. Y. Kim. Computational study of Wolff's law with trabecular architecture in the human proximal femur using topology optimization. *Journal of Biomechanics*, 41(11):2353 – 2361, 2008. doi:10.1016/j.jbiomech.2008.05.037.

[29] K. Tsubota, Y. Suzuki, T. Yamada, M. Hojo, A. Makinouchi, and T. Adachi. Computer simulation of trabecular remodeling in human proximal femur using large-scale voxel FE models: Approach to understanding Wolff's law. *Journal of biomechanics*, 42(8):1088–1094, 2009. doi:10.1016/j.jbiomech.2009.02.030.

[30] C. Boyle and I. Y. Kim. Three-dimensional micro-level computational study of Wolff's law via trabecular bone remodeling in the human proximal femur using design space topology optimization. *Journal of Biomechanics*, 44(5):935 – 942, 2011. doi:http://dx.doi.org/10.1016/j.jbiomech.2010.11.029.

[31] P. Coelho, P. Fernandes, H. Rodrigues, J. Cardoso, and J. Guedes. Numerical modeling of bone tissue adaptationa hierarchical approach for bone apparent density and trabecular structure. *Journal of Biomechanics*, 42(7):830–837, 2009. doi:http://dx.doi.org/10.1016/j.jbiomech.2009.01.020.

[32] P. Kowalczyk. Simulation of orthotropic microstructure remodelling of cancellous bone. *Journal of Biomechanics*, 43(3):563–569, 2010. doi:10.1016/j.jbiomech.2009.09.045.

[33] G. H. van Lenthe, M. Stauber, and R. Müller. Specimen-specific beam models for fast and accurate prediction of human trabecular bone mechanical properties. *Bone*, 39(6):1182–1189, 2006. doi:10.1016/j.bone.2006.06.033.

[34] K. Polgar, H. Gill, M. Viceconti, D. Murray, and J. O'Connor. Strain distribution within the human femur due to physiological and simplified loading: finite

element analysis using the muscle standardized femur model. *Proceedings of the Institution of Mechanical Engineers, Part H: Journal of Engineering in Medicine*, 217(3):173–189, 2003. doi:10.1243/095441103765212677.

[35] A. D. Speirs, M. O. Heller, G. N. Duda, and W. R. Taylor. Physiologically based boundary conditions in finite element modelling. *Journal of biomechanics*, 40(10):2318–2323, 2007. doi:10.1016/j.jbiomech.2006.10.038.

[36] G. N. Duda, M. Heller, J. Albinger, O. Schulz, E. Schneider, and L. Claes. Influence of muscle forces on femoral strain distribution. *Journal of Biomechanics*, 31(9):841 – 846, 1998. doi:http://dx.doi.org/10.1016/S0021-9290(98)00080-3.

[37] A. T. M. Phillips. The femur as a musculo-skeletal construct: a free boundary condition modelling approach. *Medical Engineering & Physics*, 31(6):673–680, 2009. doi:10.1016/j.medengphy.2008.12.008.

[38] L. Modenese, A. T. M. Phillips, and A. M. J. Bull. An open source lower limb model: Hip joint validation. *Journal of Biomechanics*, 44(12):2185–2193, 2011. doi:10.1016/j.jbiomech.2011.06.019.

[39] M. Morlock, E. Schneider, A. Bluhm, M. Vollmer, G. Bergmann, V. Mller, and M. Honl. Duration and frequency of every day activities in total hip patients. *Journal of Biomechanics*, 34(7):873–881, 2001. doi:10.1016/S0021-9290(01)00035-5.

[40] R. J. van Arkel, L. Modenese, A. T. M. Phillips, and J. R. T. Jeffers. Hip abduction can prevent posterior edge loading of hip replacements. *Journal of Orthopaedic Research*, 31(8):1172–1179, 2013. doi:10.1002/jor.22364.

[41] M. D. Klein Horsman, H. Koopman, F. C. T. Van der Helm, L. Prosé, and H. E. Veeger. Morphological muscle and joint parameters for musculoskeletal modelling of the lower extremity. *Clinical Biomechanics*, 22(2):239–247, 2007. doi:10.1016/j.clinbiomech.2006.10.003.

[42] S. L. Delp, F. C. Anderson, A. S. Arnold, P. Loan, A. Habib, C. T. John, E. Guendelman, and D. G. Thelen. OpenSim: open-source software to create and analyze dynamic simulations of movement. *IEEE Transactions on Bio-medical Engineering*, 54(11):1940–1950, 2007. doi:10.1109/TBME.2007.901024.

[43] G. Wu, S. Siegler, P. Allard, C. Kirtley, A. Leardini, D. Rosenbaum, M. Whittle, D. D. D'Lima, L. Cristofolini, and H. Witte. ISB recommendation on definitions of joint coordinate system of various joints for the reporting of human joint motion – part i: ankle, hip, and spine. *Journal of Biomechanics*, 35(4):543–548, 2002. doi:10.1016/S0021-9290(01)00222-6.

[44] S. Martelli, F. Taddei, D. Testi, S. Delp, and M. Viceconti. Nms builder: an application to personalize nms models. In *Proceedings of the 23rd Congress of the International Society of Biomechanics*, 2011.

[45] H. Gray. *Anatomy of the human body*. Lea & Febiger, 1918.

[46] W. Platzer. *Color Atlas of Human aAnatomy: Locomotor System*, volume 1. Thieme, 6 edition, 2008. ISBN-13: 978-3135333069.

[47] M. Viceconti, M. Ansaloni, M. Baleani, and A. Toni. The muscle standardized femur: a step forward in the replication of numerical studies in biomechanics. *Proceedings of the Institution of Mechanical Engineers, Part H: Journal of Engineering in Medicine*, 217(2):105–110, 2003. doi:10.1243/09544110360579312.

[48] R. A. Brand, D. R. Pedersen, D. T. Davy, G. M. Kotzar, K. G. Heiple, and V. M. Goldberg. Comparison of hip force calculations and measurements in the same patient. *Journal of Arthroplasty*, 9(1):45–51, 1994. doi:10.1016/0883-5403(94)90136-8.

[49] L. Modenese, A. Gopalakrishnan, and A. T. M. Phillips. Application of a falsification strategy to a musculoskeletal model of the lower limb and accuracy of the predicted hip contact force vector. *Journal of Biomechanics*, 46(6):1193 – 1200, 2013. doi:10.1016/j.jbiomech.2012.11.045.

[50] A. Barre and S. Armand. Biomechanical toolkit: Open-source framework to visualize and process biomechanical data. *Computer Methods and Programs in Biomedicine*, 144(1):80–87, 2014. doi:10.1016/j.cmpb.2014.01.012.

[51] R. Dumas, L. Cheze, and J.-P. Verriest. Adjustments to McConville et al. and Young et al. body segment inertial parameters. *Journal of biomechanics*, 40(3):543–553, 2007. doi:10.1016/j.jbiomech.2006.02.013.

[52] T. Lu and J. J. OConnor. Bone position estimation from skin marker coordinates using global optimisation with joint constraints. *Journal of biomechanics*, 32(2):129–134, 1999. doi:10.1016/S0021-9290(98)00158-4.

[53] L. Modenese and A. T. M. Phillips. Prediction of hip contact forces and muscle activations during walking at different speeds. *Multibody System Dynamics*, 28(1-2):157–168, 2012. doi:10.1007/s11044-011-9274-7.

[54] K. M. Steele, M. S. DeMers, M. S. Schwartz, and S. L. Delp. Compressive tibiofemoral force during crouch gait. *Gait & Posture*, 35:556–560, 2012. doi:10.1016/j.gaitpost.2011.11.023.

[55] C. H. Turner, J. Rho, Y. Takano, T. Y. Tsui, and G. M. Pharr. The elastic properties of trabecular and cortical bone tissues are similar: results from two microscopic measurement techniques. *Journal of Biomechanics*, 32(4):437–441, 1999. doi:10.1016/S0021-9290(98)00177-8.

[56] G. Bergmann, G. Deuretzbacher, M. Heller, F. Graichen, A. Rohlmann, J. Strauss, and G. N. Duda. Hip contact forces and gait patterns from routine activities. *Journal of biomechanics*, 34(7):859–871, 2001. doi:10.1016/S0021-9290(01)00040-9. HIP98 dataset available from www.orthoload.com.

[57] A. Aamodt, J. Lund–Larson, J. Eine, E. Andersen, P. Benum, and O. Schnell Husby. In vivo mmeasurement show tensile axial strain in the proximal lateral aspect of the human femur. *Journal of Orthopaedic Research*, 15:927–931, 1997.

[58] P. Stephenson and B. B. Seedhom. Cross-sectional geometry of the human femur in the mid-third region. *Proceedings of the Institution of Mechanical Engineers, Part H: Journal of Engineering in Medicine*, 213(2):159–166, 1999. doi:10.1243/0954411991534889.

[59] G. Treece, A. Gee, P. Mayhew, and K. Poole. High resolution cortical bone thickness measurement from clinical CT data. *Medical Image Analysis*, 14(3):276–290, 2010. doi:10.1016/j.media.2010.01.003.

[60] M. Singh, A. Nagrath, and P. Maini. Changes in trabecular pattern of the upper end of the femur as an index of osteoporosis. *The Journal of Bone & Joint Surgery*, 52(3):457–467, 1970. PMID: 5425640.

[61] H. A. Kim, G. J. Howard, and J. L. Cunningham. Do trabeculae of femoral head represent a structural optimum? In *13th International Conference on Biomedical Engineering*, volume 23 of *IFMBE Proceedings*, pages 1636–1639. Springer Berlin Heidelberg, 2009.

[62] R. Garden. The structure and function of the proximal end of the femur. *Journal of Bone & Joint Surgery, British Volume*, 43(3):576–589, 1961.

[63] H. Takechi. Trabecular architecture of the knee joint. *Acta Orthopaedica Scandinavica*, 48:673–681, 1977. doi:10.3109/17453677708994816.

[64] D. W. Wagner, K. Divringi, C. Ozcan, M. Grujicic, B. Pandurangan, and A. Grujicic. Combined musculoskeletal dynamics/structural finite element analysis of femur physiological loads during walking. *Multidiscipline Modeling in Materials and Structures*, 6:417–437, 2010. doi:10.1108/15736101011095118.

[65] M. Cronskär, J. Rasmussen, and M. Tinnsten. Combined finite element and multibody musculoskeletal investigation of a fractured clavicle with reconstruction plate. *Computer Methods in Biomechanics and Biomedical Engineering*, 2013. doi:10.1080/10255842.2013.845175. In press, accepted manuscript.

[66] G. T. Yamaguchi. *Dynamic Modeling of Musculoskeletal Motion: a Vectorised Approach for Biomechanical Analysis in Three Dimensions*. Springer, 2005. ISBN-13: 978-0387287041.

[67] I. R. Grosse, E. R. Dumont, C. Coletta, and A. Tolleson. Techniques for modeling muscle-induced forces in finite element models of skeletal structures. *The Anatomical Record: Advances in Integrative Anatomy and Evolutionary Biology*, 290(9):1069–1088, 2007. doi:10.1002/ar.20568.

[68] P. Favre, C. Gerber, and J. G. Snedeker. Automated muscle wrapping using finite element contact detection. *Journal of Biomechanics*, 43(10):1931–1940, 2010. doi:10.1016/j.jbiomech.2010.03.018.

[69] J. P. Halloran, M. Ackermann, A. Erdemir, and A. J. van den Bogert. Concurrent musculoskeletal dynamics and finite element analysis predicts altered gait patterns to reduce foot tissue loading. *Journal of Biomechanics*, 43(14):2810–2815, 2010. doi:10.1016/j.jbiomech.2010.05.036.

[70] M. Kunze, A. Schaller, H. Steinke, R. Scholz, and C. Voigt. Combined multi-body and finite element investigation of the effect of the seat height on acetabular implant stability during the activity of getting up. *Computer Methods and Programs in Biomedicine*, 105(2):175–182, 2012. doi:10.1016/j.cmpb.2011.09.008.

[71] T. Hildebrand, A. Laib, R. Müller, J. Dequeker, and P. Regsegger. Direct three-dimensional morphometric analysis of human cancellous bone: Microstructural data from spine, femur, iliac crest, and calcaneus. *Journal of Bone and Mineral Research*, 14(7):1167–1174, 1999. doi:10.1359/jbmr.1999.14.7.1167.

[72] A. Phillips, P. Pankaj, C. Howie, A. Usmani, and A. Simpson. Finite element modelling of the pelvis: Inclusion of muscular and ligamentous boundary conditions. *Medical Engineering & Physics*, 29(7):739 – 748, 2007. doi:10.1016/j.medengphy.2006.08.010.

[73] S. Martelli, M. E. Kersh, A. G. Schache, and M. G. Pandy. Strain energy in the femoral neck during exercise. *Journal of Biomechanics*, 2014. doi:10.1016/j.jbiomech.2014.03.036. In press, accepted manuscript.

List of Figures

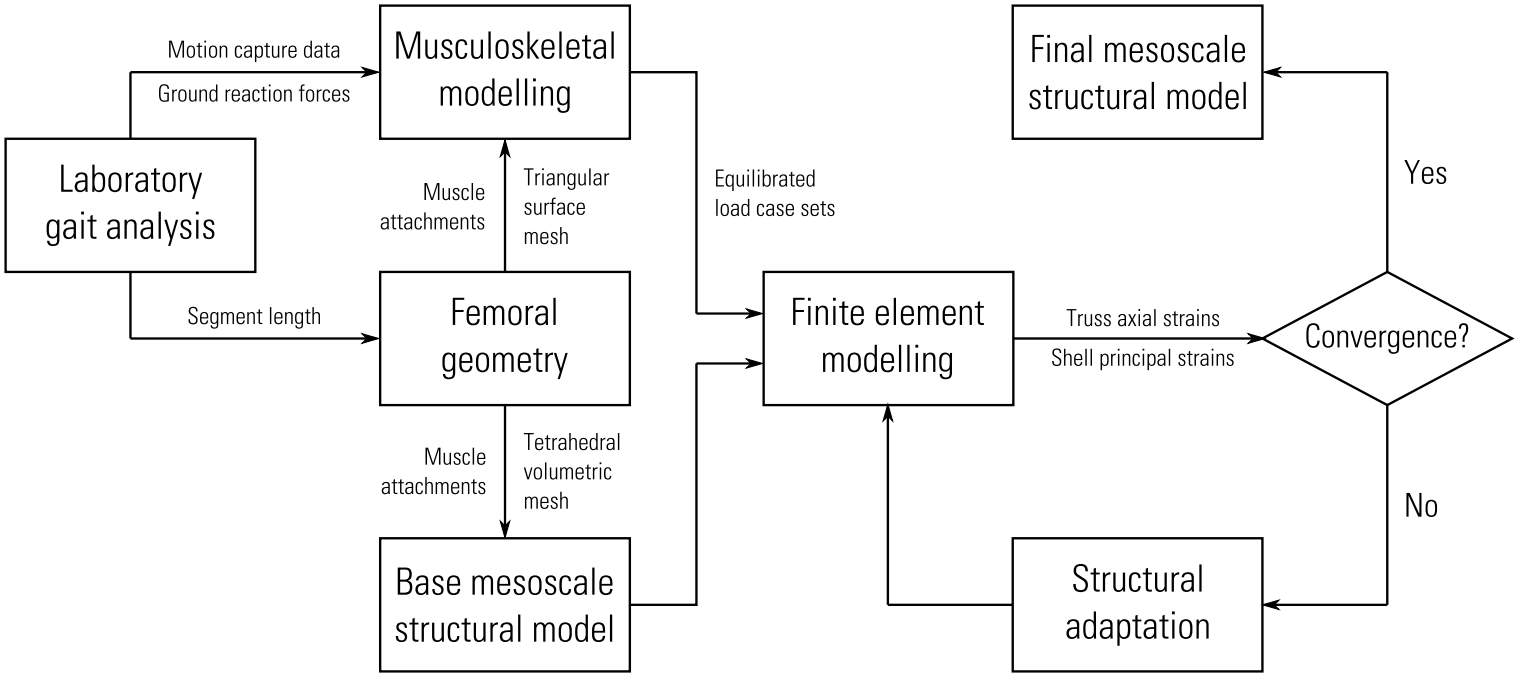

Figure 1: Musculoskeletal and finite element modelling framework

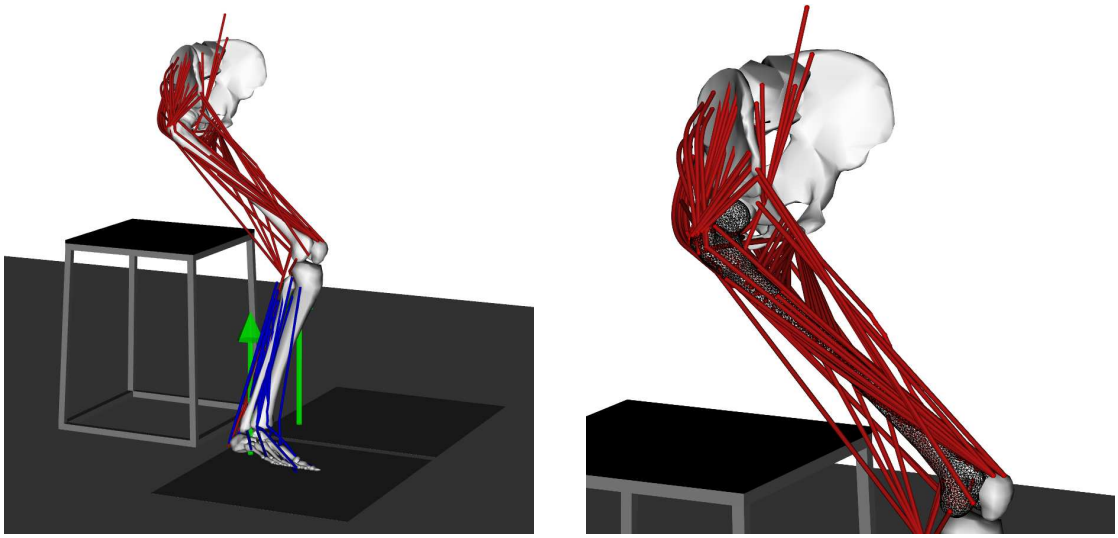

(a) (b)

Figure 2: The developed musculoskeletal model, a) during sit-to-stand, b) close up of the femoral mesh identical to that used in the FE simulations. Forces from those muscles highlighted in red are applied in the FE simulations. Ground reaction forces beneath each foot are shown. Wrapping surfaces are omitted for clarity.

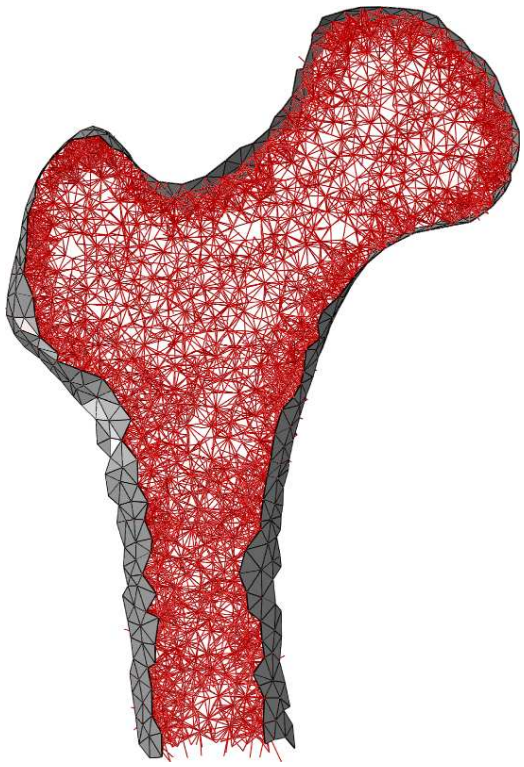

Figure 3: 2.5mm slice of the proximal femur for the base model. Shell elements representing cortical bone are shown in grey, truss elements representing trabecular bone are shown in red.

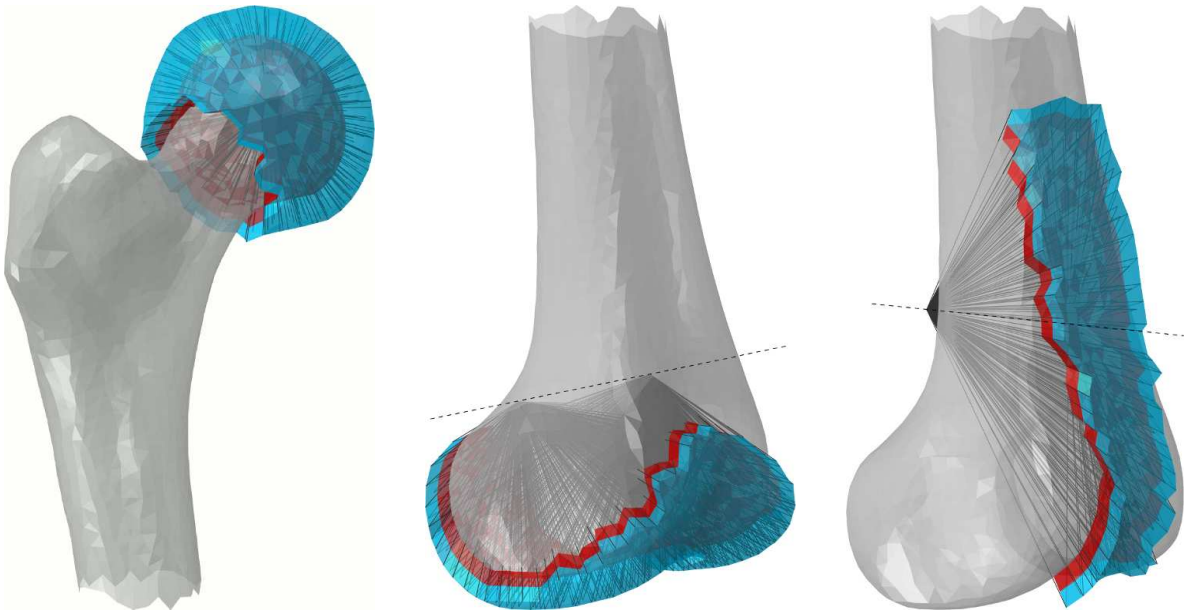

(a) (b) (c)

Figure 4: Load applicators at the, a) hip, b) knee, c) patellofemoral joints. Shell elements representing cortical bone and the wedge elements of the applicators are shown as semi-transparent to highlight the truss elements linking the applicator constructs to the hip joint centre, the knee and patellofemoral joint axes respectively. Dashed lines show the joint axes for the knee and patellofemoral joints.

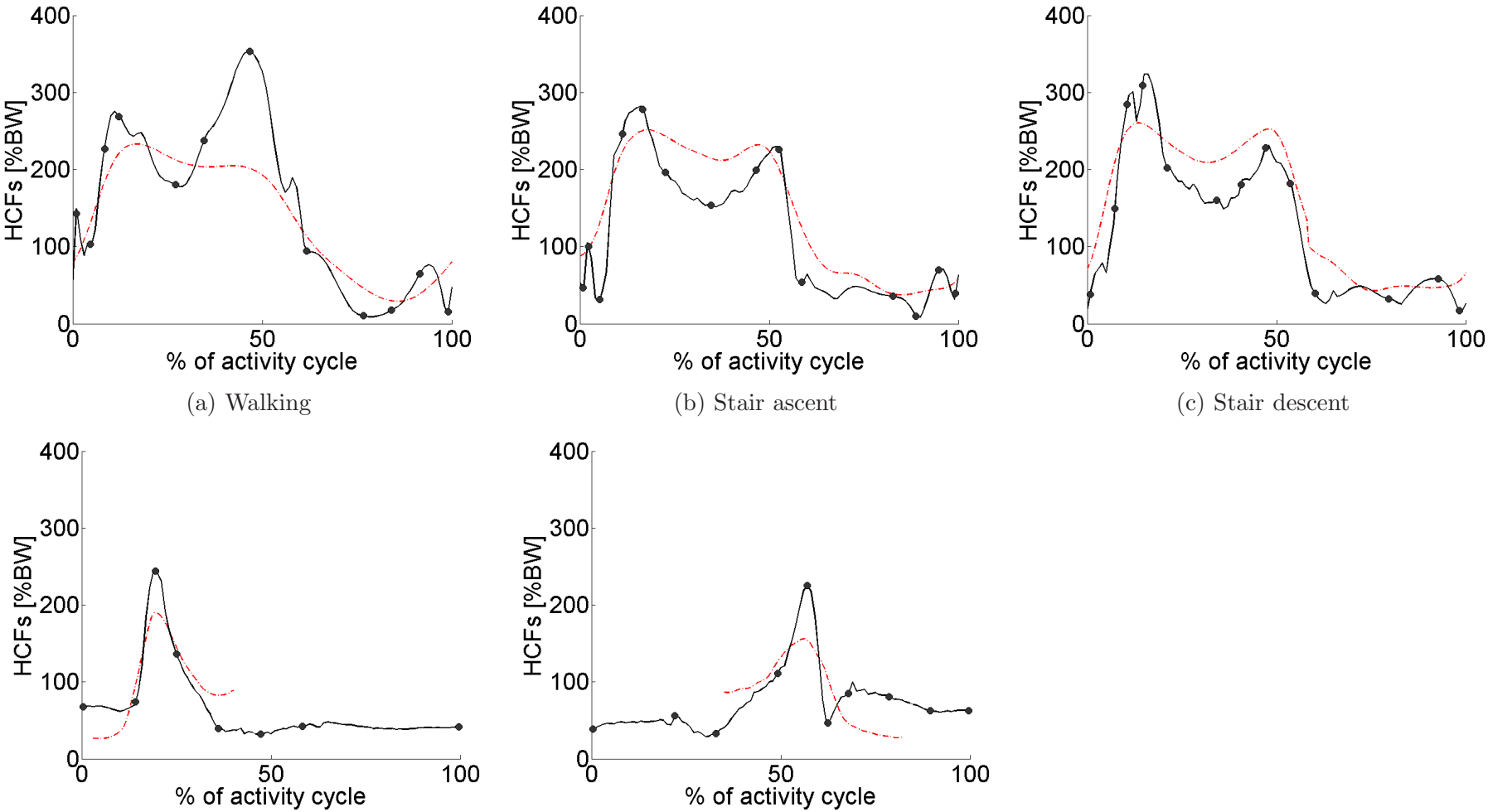

(a) Walking

(b) Stair ascent

(c) Stair descent

(d) Sit-to-stand

(e) Stand-to-sit

Figure 5: Hip JCFs derived from the musculoskeletal model for single cycles of (a) walking, (b) stair ascent, (c) stair descent, (d) sit-to-stand, (e) stand-to-sit, are shown as black solid lines. Selected frames from each activity, used in the FE simulations, are indicated using solid circles. Average hip JCFs across all subjects for all trials, as recorded and reported by Bergmann et al. [56] for the same activities, are shown as red dash-dot lines (full details of the customised averaging process are available on the HIP98 dataset accompanying [56]). Due to differences in the selection of the start and finish points of some activity cycles, the average hip JCFs reported by Bergmann et al. [56] for these activities are shifted (stair descent) or plotted over approximately corresponding periods (sit-to-stand and stand-to-sit) for easier visual comparison.

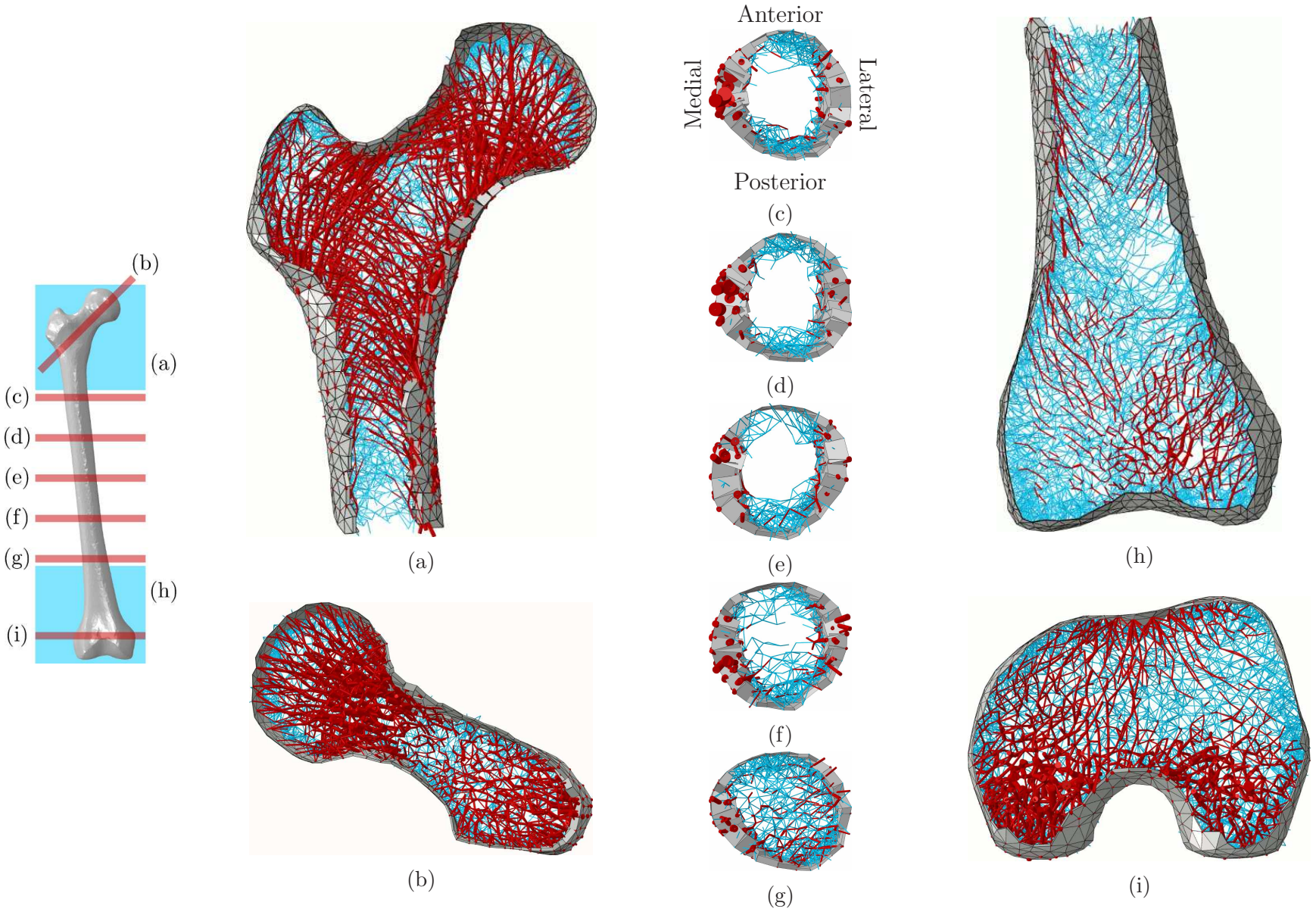

Figure 6: Selected 5mm slices for the converged mesoscale structural model subjected to a single load case taken at maximum hip JCF during walking. Shell elements representing cortical bone are shown in grey, truss elements representing trabecular bone with a radius $r > 0.1$mm are shown in red, truss elements with a radius $r = 0.1$mm are shown in the background in blue. Truss elements with a radius $r = 1\mu$m are omitted for clarity.

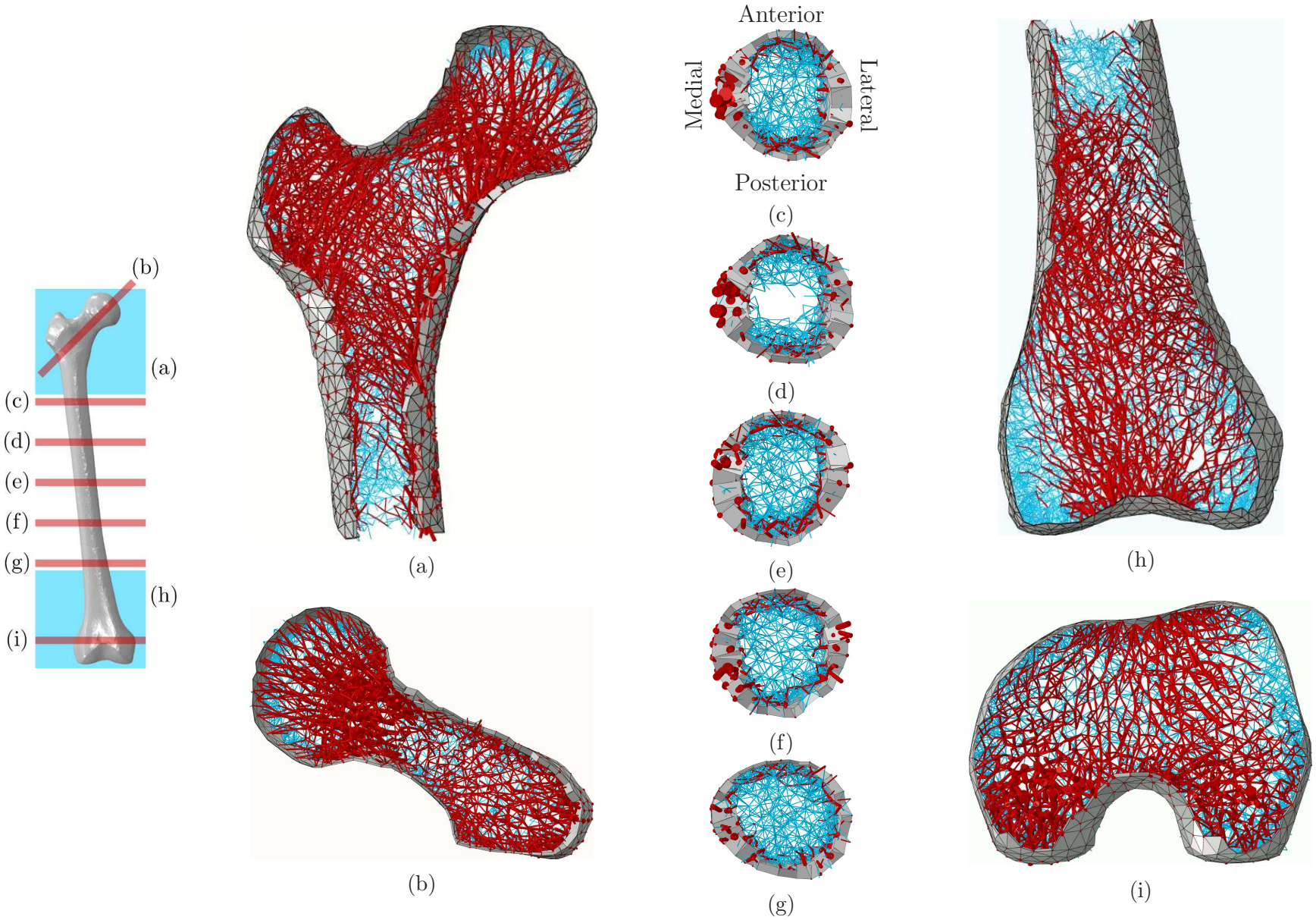

Figure 7: Selected 5mm slices for the converged mesoscale structural model subjected to the full loading regime. Shell elements representing cortical bone are shown in grey, truss elements representing trabecular bone with a radius $r > 0.1$mm are shown in red, truss elements with a radius $r = 0.1$mm are shown in the background in blue. Truss elements with a radius $r = 1\mu$m are omitted for clarity.

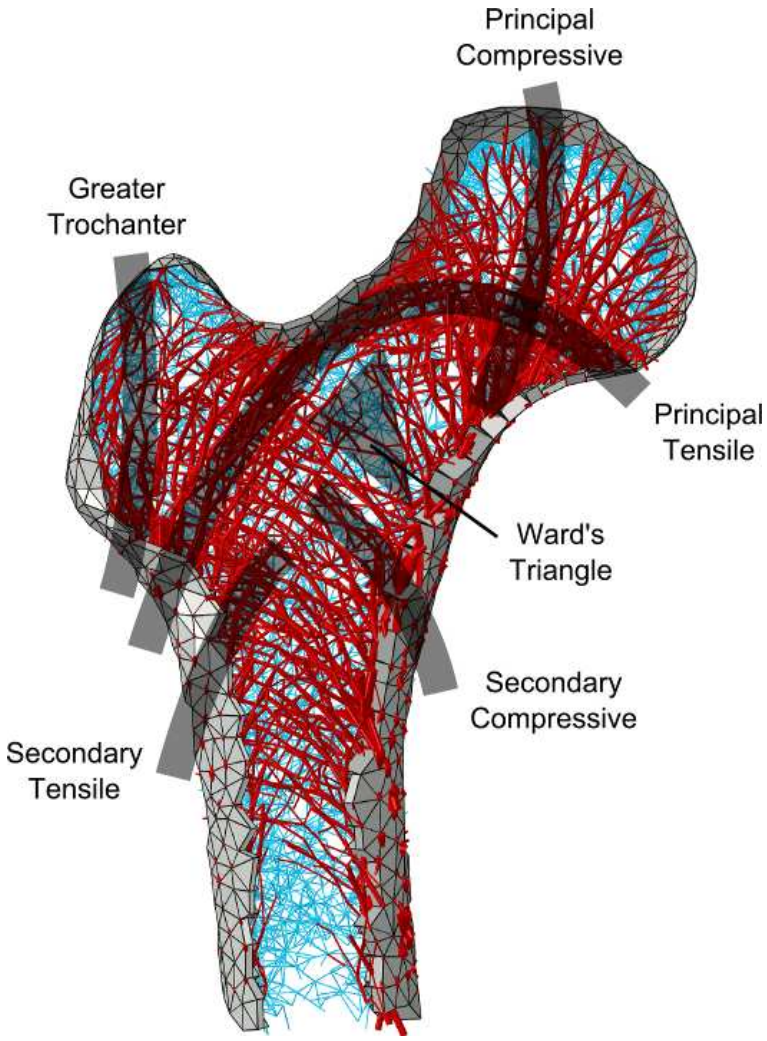

Figure 8: 5mm slice for the converged mesoscale structural model subjected to a single load case taken at maximum hip JCF during walking (as shown in Fig. 6a), highlighting the five normal groups of trabeculae identified by Singh et al. [60] and Ward's triangle.

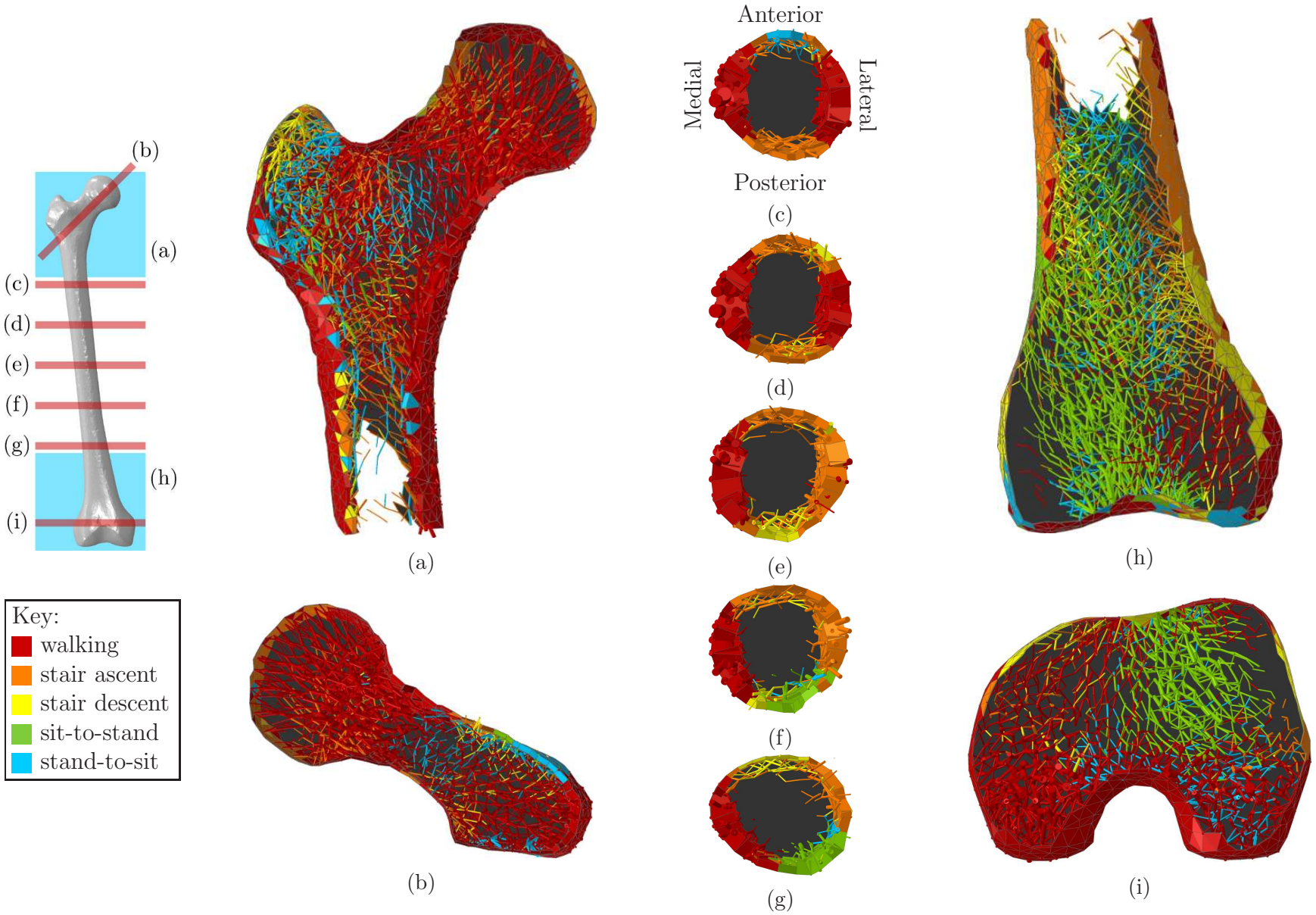

Figure 9: Selected 5mm slices for the converged mesoscale structural model subjected to the full loading regime. Shell and truss elements are colour-mapped according to the activity most influential in determining their geometry. Truss elements with a radius $r \leq 0.1$mm are omitted for clarity.

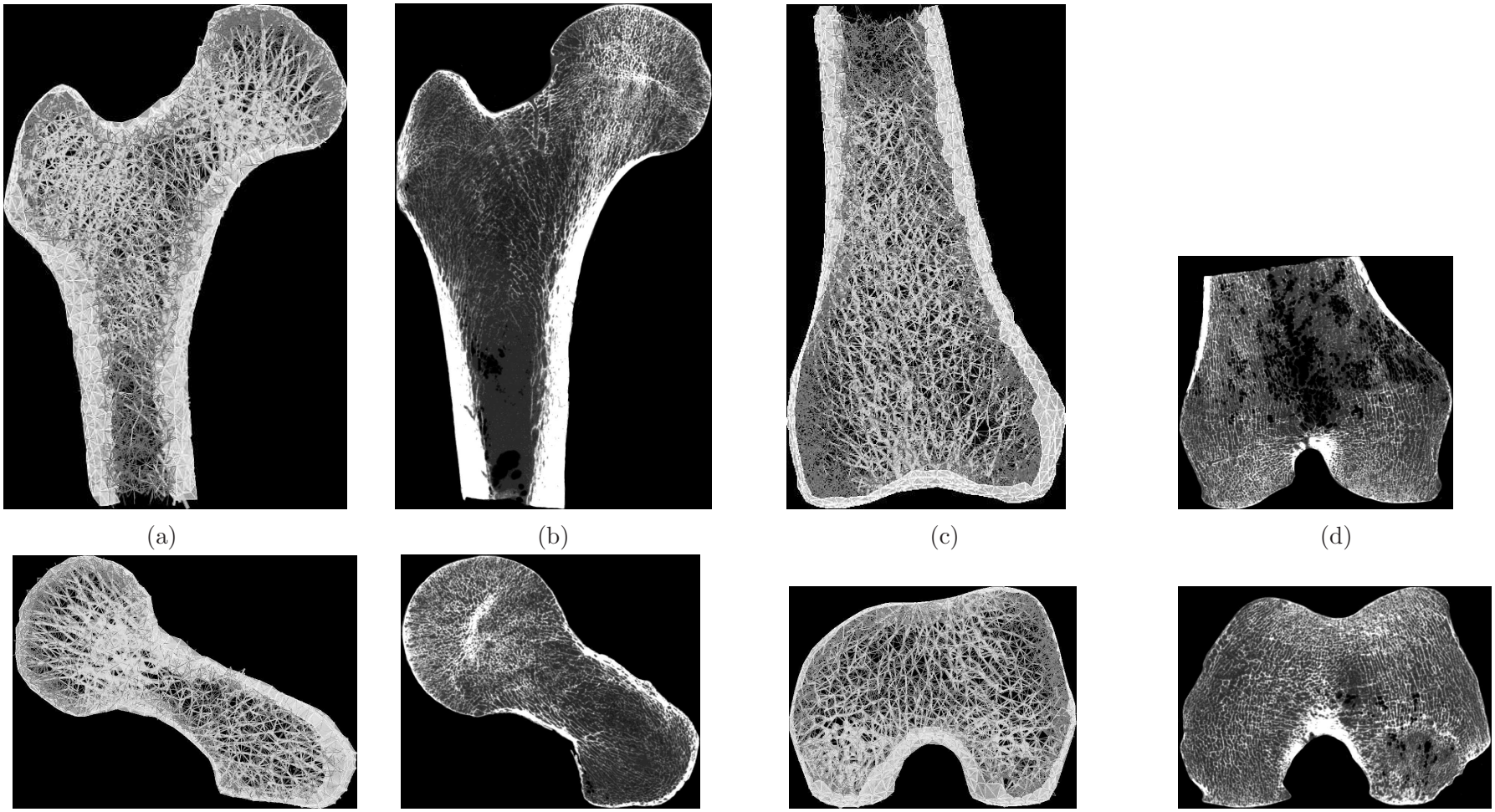

(a) (b) (c) (d)

(e) (f) (g) (h)

Figure 10: Selected 5mm slices for the altered thickness converged mesoscale structural model subjected to the full loading regime (a, c, e, g), shown alongside corresponding μCT slices (b, d, f, h). Shell and truss elements with a radius $r > 0.1$mm are coloured light grey. Truss elements with a radius $r = 0.1$mm are coloured dark grey. Truss elements with a radius $r = 1\mu$m are omitted for clarity. All slices are shown as semi-transparent to highlight the structure through the depth of the slice.

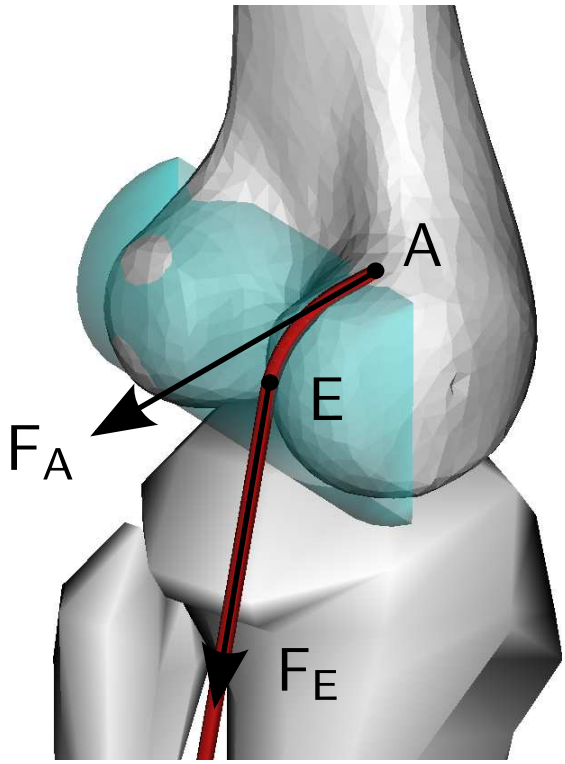

Figure 11: Anatomical and effective lines of action, force vectors $\mathsf{F_A}$ and $\mathsf{F_E}$, and insertions A and E respectively, for the gastrocnemius medialis muscle.